Measurement Science
and Technology

ACCEPTED MANUSCRIPT • OPEN ACCESS

Experimental Optimization of a Multiple-Reflection System for Acoustic Material Property Measurement

To cite this article before publication: Suzi Liang *et al* 2025 *Meas. Sci. Technol.* in press https://doi.org/10.1088/1361-6501/ae1855

Experimental Optimisation of a Multiple-Reflection System for Acoustic Material Property Measurement

Suzi Liang[1]‡, Rui Xu[1], Morgan Roberts[1], Benjamin T Cox[1], Bradley E Treeby[1], Eleanor Martin[1]

[1]Department of Medical Physics and Biomedical Engineering, University College London, London WC1E 6BT, UK

Abstract. Knowledge of the acoustic properties of materials is critical for many applications of acoustics. Common methods for measurement of acoustic material properties include the through transmission substitution-insertion method (SIM), and the multiple-reflection method (MRM). However, the accuracy and uncertainty of MRM measurements have not been evaluated as widely as for SIM. This study investigates the impact of system compressional force, buffer rod diameter, and buffer rod and specimen surface conditions on accuracy and repeatability of MRM measurements of attenuation coefficient and longitudinal sound velocity of 3D printed specimens, validated against SIM measurements. Measurement accuracy and repeatability improved as system compression was increased, with attenuation coefficients measured by SIM and MRM at 0.5 MHz converging to within 0.1 dB/cm (1.6 ± 0.1 dB/cm vs 1.7 ± 0.2 dB/cm) for the RGDA8625 material. A buffer rod of at least twice the diameter of the transducer was required for agreement between the two methods, differences of >40% were measured with narrower buffer rods. The buffer rod and specimen should be sufficiently flat and well-polished to minimise errors. These findings may guide future system design and optimisation, and suggest that experimental convergence should be verified on setup. This may aid the standardisation of measurement protocols, helping to improve accuracy and repeatability of acoustic material property measurements.

Keywords: acoustic material property, measurement optimisation, multiple-reflection method, measurement validation, attenuation coefficient, longitudinal sound velocity

‡ Corresponding author: rmapsl0@ucl.ac.uk

1. Introduction

Knowledge of acoustic properties of materials underpins technological advances across diverse applications, from Non-Destructive Testing (NDT) [1–4] and subharmonic-aided pressure estimation (SHAPE) [5–8], to medical ultrasound [9–12], underwater acoustic detection [13, 14], and food industry applications [15, 16]. Among the methods for measuring sound velocity and attenuation coefficient, the substitution-insertion method (SIM) and multiple-reflection method (MRM) are most widely used, each offering distinct advantages for different measurement scenarios.

SIM measures acoustic properties by comparing reference waveforms propagated through a reference medium (usually water) with those obtained after specimen insertion [17, 18]. Extensively used for biologically relevant, liquid and soft solid specimens, sources of uncertainty in SIM measurements are well understood, including scanning tank dimensions, alignment factors, and temperature control [19, 20]. Established mitigation approaches include using multiple specimen thicknesses to correct for interfacial losses during attenuation coefficient measurement [19, 21].

MRM utilizes a solid buffer rod to couple the acoustic source with the specimen, eliminating direct contact and water medium requirements [22, 23]. This can protect transducers from harsh specimen environments and enables derivation of attenuation coefficients from reflected signals without requiring prior knowledge of buffer rod properties. This independence from reference values makes MRM suitable for extreme conditions, previously demonstrated in measurements of molten glass at 1000-1200°C [24], frozen materials to -50°C [12, 25], and high ambient pressures up to 7 GPa [26].

However, compared to SIM, MRM measurement accuracy and uncertainty sources have not been evaluated as extensively. Several factors influence the accuracy and precision of MRM measurements, including selection of buffer rod material to minimize attenuation and impedance mismatch, optimal specimen thickness, buffer rod length for signal separation, and incorporation of temperature-dependent buffer rod parameters. [22]. Previous enhancement efforts include diffraction correction [27], simulation-based buffer rod diameter optimisation [28], methods to reduce buffer rod length [29], and dual-transducer configurations [30]. Despite these efforts, further understanding of the influence of several aspects of MRM system design and experimental procedures is still needed to ensure high-quality acoustic measurements.

This study investigates three key aspects: the impact of compressional force, buffer rod diameter, and surface conditioning effects for both buffer rod and specimen. While coupling gels aid component contact, the optimal compressional force for required for accurate, repeatable MRM measurements requires investigation. Buffer rod diameter must be optimised relative to transducer and specimen dimensions to eliminate boundary reflection interference. Although theoretical calculations suggest buffer rods should be at least twice the transducer diameter to minimize side-wall effects [31], experimental validation is necessary given setup specific variations in field divergence. Surface conditioning is critical, as reflection coefficients have been observed

to vary nine-fold between surfaces with roughness 2 times versus 100 times smaller than the wavelength [32].

Acoustic property characterisation of materials under extreme conditions is critical for developing ultrasound rewarming technology [33,34] and other emerging applications, so this study aimed to quantify the impact of the aforementioned factors to improve the MRM system and measurements. The impact of these factors were investigated by measuring the attenuation coefficients and sound velocities of 3D printed specimens using a custom MRM system. The specimens were chosen as their acoustic properties have been previously measured [35] using SIM. During the quantification process, this MRM system was optimised to minimise the influence of each experimental factor to reduce measurement uncertainty for improved repeatability, and to enhance accuracy, which was assessed by benchmarking against SIM measurements. A single specimen material was used for this optimisation at a frequency of 0.5 MHz. The generalisability of the optimised system was then validated using two additional specimens at both 0.5 and 1 MHz. This frequency range was chosen due to the intended use of the system for measuring the acoustic properties of frozen materials in future work on ultrasonic rewarming of cryopreserved tissues [33,34] which has so far employed frequencies in this range.

2. Methods

2.1. Multiple-Reflection Method (MRM) Calculation Principle

Attenuation coefficient measurement using the MRM relies on the analysis of the physical relationship between the transmitted pulse $p_0(t)$ and multiple echoes $p_1(t)$, $p_2(t)$, and $p_3(t)$, reflected from buffer rod and specimen interfaces. As illustrated in Fig. 1, $p_0(t)$ is the initial pulse emitted by the transducer. The first echo reflected from the far surface of the buffer rod is $p_1(t)$, then $p_2(t)$ and $p_3(t)$ are the first and second echoes from the far surface of the specimen, respectively. In the frequency domain, the amplitude spectrum of the echoes $p_{1-3}(t)$ can be written as a function of the transmitted pulse $p_0(t)$, the reflection coefficients and the amplitude loss during propagation [36,37]:

$$A_1(f) = A_0(f)\ R_{12}\ E_1, \tag{1}$$

$$A_2(f) = A_0(f)\ T_{21}\ R_{23}\ T_{12}\ E_1\ E_2, \tag{2}$$

$$A_3(f) = A_0(f)\ T_{21}\ R_{23}\ R_{21}\ R_{23}\ T_{12}\ E_1\ E_2^2, \tag{3}$$

$$R_{ij} = -R_{ij}, \tag{4}$$

$$T_{ij} = 1 - R_{ij}, \tag{5}$$

$$E_i = \exp(-2\ a_i\ d_i), \tag{6}$$

where $A_{0-3}(f)$ are the magnitude spectra of $p_{0-3}(t)$ obtained by fast Fourier Transform (FFT), respectively. R_{ij} and T_{ij} are the amplitude reflection and transmission coefficients from material i to material j, where the buffer rod, specimen and air are

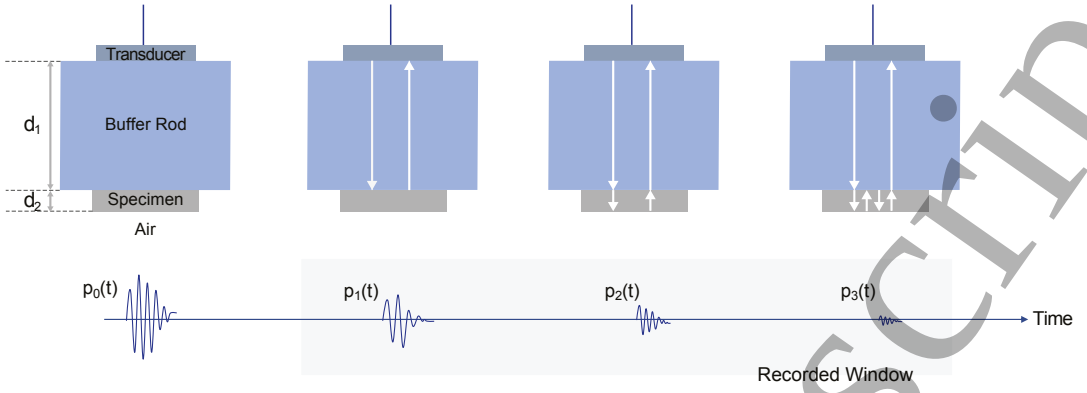

Figure 1. Schematic showing transmitted and reflected ultrasonic waveforms in the multiple-reflection method (MRM) for attenuation coefficient calculation. The waveforms include the initial transmitted pulse $p_0(t)$, the first reflection $p_1(t)$ from the buffer rod end, and subsequent reflections $p_2(t)$ and $p_3(t)$ from the specimen's distal surface. The buffer rod material, and hence sound velocity, and geometry were chosen to ensure that $p_3(t)$ would arrive before the second echo reflected from the buffer rod–specimen interface to avoid waveform mixing.

respectively represented by indices 1, 2 and 3. For instance, R_{12} represents the amplitude reflection coefficient of a waveform reflected from the material 1 - material 2 interface (buffer rod to specimen interface). E_i is the amplitude loss of the waveform during its two-way propagation in material i, d_i is the length of material i in cm and a_i is the attenuation coefficient of the material in Np/cm.

Using these formulae, the attenuation coefficient of the specimen can be calculated from A_1, A_2 and A_3 without prior knowledge of the buffer rod attenuation coefficient or the buffer rod-to-specimen reflection coefficient, and is given by

$$a_2(f) = -\frac{1}{2\ d_2} \ln\left|\frac{A_2\ \sqrt{A_3} + \sqrt{A_1}\ A_3}{\sqrt{A_1}\ A_2}\right|. \tag{7}$$

For this expression to be valid, the reflection coefficient R_{23} must approach -1. The reflection coefficient at normal incidence [38] is calculated via the acoustic impedance contrast of adjoining materials and is given by

$$R_{ij} = \frac{Z_j - Z_i}{Z_i + Z_j} = \frac{\rho_j\ c_j - \rho_i\ c_i}{\rho_i\ c_i + \rho_j\ c_j}, \tag{8}$$

where $Z_{i,j}$ is the acoustic impedance of material i, j, defined as the product of its density $\rho_{i,j}$ and sound velocity $c_{i,j}$. The acoustic impedance of air is approximately 400 Rayl, and the buffer rod impedance is 3.5 MRayl calculated using sound velocity of 2357 m/s (measured in-house) and density of 1120 kg/m^3 [39], so the reflection coefficient at the specimen and air interface, R_{23}, is approximately equal to -1.

In practice, if A_3 is heavily attenuated and too small to measure, the reflection coefficient R_{12} between the buffer rod and specimen surface could be employed to calculate the attenuation coefficient of the specimen and is given by

$$a_2 = -\frac{1}{2\ d_2}\ \ln\left|\frac{A_2}{A_1}\ \frac{R_{12}}{(1 - R_{12}^2)}\right|. \tag{9}$$

The theoretical value of R_{12} can be calculated using Eq. 8. In practice, R_{12} can be measured by comparing the signal before and after specimen insertion. From Eq.1-3, the amplitude of the signal reflected from the interface between the buffer rod and air can be expressed as

$$A_{air}(f) = A_0(f)\ R_{13}\ E_1. \tag{10}$$

As for R_{23}, R_{13} can be approximated as -1, then R_{12} can be calculated by

$$R_{12}(f) = -\frac{A_1(f)}{A_{air}(f)}. \tag{11}$$

The a_2 calculated from either Eq. 7 or 9 is expressed in units of Np/cm. This can be subsequently converted to the more commonly used unit dB/cm, using the relationship $1\,\mathrm{Np} = 8.686\,\mathrm{dB}$. The sound velocities can be calculated using the Time-of-Flight (TOF) method [40], where the velocities are calculated by the propagation time determined from the reflected waveforms which travel a known distance calculated as

$$c = d/t, \tag{12}$$

where c is the sound velocity, d is the travel distance, and t is the time of flight.

2.2. Multiple-Reflection Method Measurement Setup

A single-element planar transducer (V389, Panametrics-NDTTM, Olympus NDT, Waltham, MA, USA) serves as both transmitter and receiver, with a center frequency of 0.5 MHz and a diameter of 39.1 mm. The buffer rod, a cylindrical piece of Nylon 6.6, was shaped, flattened, and polished using a Colchester Mascot 1600 lathe, to a diameter of 185 mm and thickness of 101 mm. The test specimen used for optimisation of the setup was a disk of RGDA8625 material printed using a Stratasys J835 printer (Stratasys, Edina, MN, US) with diameter of 60 mm and thickness of 8 mm. To ensure optimal coupling, a water-gel coupling agent (Anagel, Ana Wit Ltd., Surrey, UK) was applied to all interfaces within the transducer-buffer rod-specimen assembly. The components of the MRM system were centrally aligned using 3D printed holders and secured using M8 bolts on either side, each with a length of 80 mm (Fig. 2a).

The transducer was connected to a pulser-receiver (DPR300, JSR Ultrasonics, Pittsford, NY, USA) set in echo mode with 10 dB gain, pulse repetition frequency 100 Hz, low-pass filter set at 5 MHz, pulse amplitude level 10 (corresponding to ∼297 V), operating in low impedance mode at energy level 4. Acoustic signals received by the transducer were acquired and displayed using a DSO-X 3024A oscilloscope (Keysight Technologies, Santa Rosa, CA, USA), with a 4 GHz sampling rate and 128 averages (Fig. 2b). To calculate the attenuation coefficient, paired waveforms were recorded both in the presence and absence of the specimen (Fig. 2c). This procedure was repeated five times for every condition, with the setup dismantled and reassembled between each iteration.

The recorded acoustic signals were processed in `MATLAB` (The Mathworks Inc., Natick, USA). The individual pulses were cropped from the waveform traces, then the position of the temporal minimum voltage was identified for each. Subsequently, a Tukey window with a taper ratio of 0.1 was applied. For the 500 kHz data, the window started $sim3\mu$s before the temporal minimum and ended after the end of the pulse, which was identified by the occurrence of the third peak (i.e., the last positive-going half-cycle). Following this, the single-sided magnitude spectrum $A(f)$ was obtained by FFT. As observed in Fig. 2c, the third echo amplitude A_3, corresponding to the second internal reflection $p_3(t)$, was significantly attenuated. Equation 7 requires A_3 for calculation, but since this is small in this case, the attenuation coefficient was instead determined using Eq. 9, which requires only A_1, A_2, as well as the measured reflection coefficient R_{12} calculated from Eq. 11.

Additionally, the sound velocity of the specimen was calculated from each measurement using the ToF method [12, 40], where the velocity was determined from the arrival time of the received waveforms and the known propagation distance. It is possible to determine the time delay using various time-picking criteria [12]. For this analysis, three time-picking criteria were employed for comparison: the point of waveform onset, and the time corresponding to the peak maximum and minimum voltages of the waveforms. Waveform onset was determined using a threshold set at two standard deviations above the mean noise level [41]. For each time-picking criterion, the mean and standard deviation of the resulting velocities were calculated from five repeated measurements. Uncertainty in propagation distance was also incorporated from the standard deviation of three measurements of specimen thickness.

2.3. Substitution-insertion method (SIM) Reference Measurements

The SIM was used to obtain reference measurements for validation of the accuracy of measurements made with the optimised MRM system. The measurement set-up and specimens used here have been previously and are described in [35]. Fig. 3a shows the measurement setup with the specimen, transducer and hydrophone centrally aligned in a tank filled with deionised water. The planar transducer used in the MRM system was used here to generate acoustic signals. It was driven with a 0.5 MHz, 1 cycle sinusoidal pulse, generated by an arbitrary waveform generator (Keysight 33500B, Santa Rosa, CA, USA) and amplified by a RF amplifier (1020L, E&I, Rochester, NY, USA) with 53 dB gain. The receiver was a 5 mm diameter PVDF sensor (Precision Acoustics, Dorset, UK), aligned to the beam axis in the far field of the transducer. To account for interfacial losses in the SIM measurements, at least two specimens of different thicknesses are required [19]. For the RGDA8625 material, specimens of 4 and 8 mm thickness were used. To assess measurement repeatability and potential errors from e.g. diffraction effects [21], four repeat sets of measurements were conducted under slightly different conditions: at two transmitter-receiver distances (30 and 35 cm) and two pulse voltage amplitudes (100 and 110 mV) for each specimen. These signals were amplified before

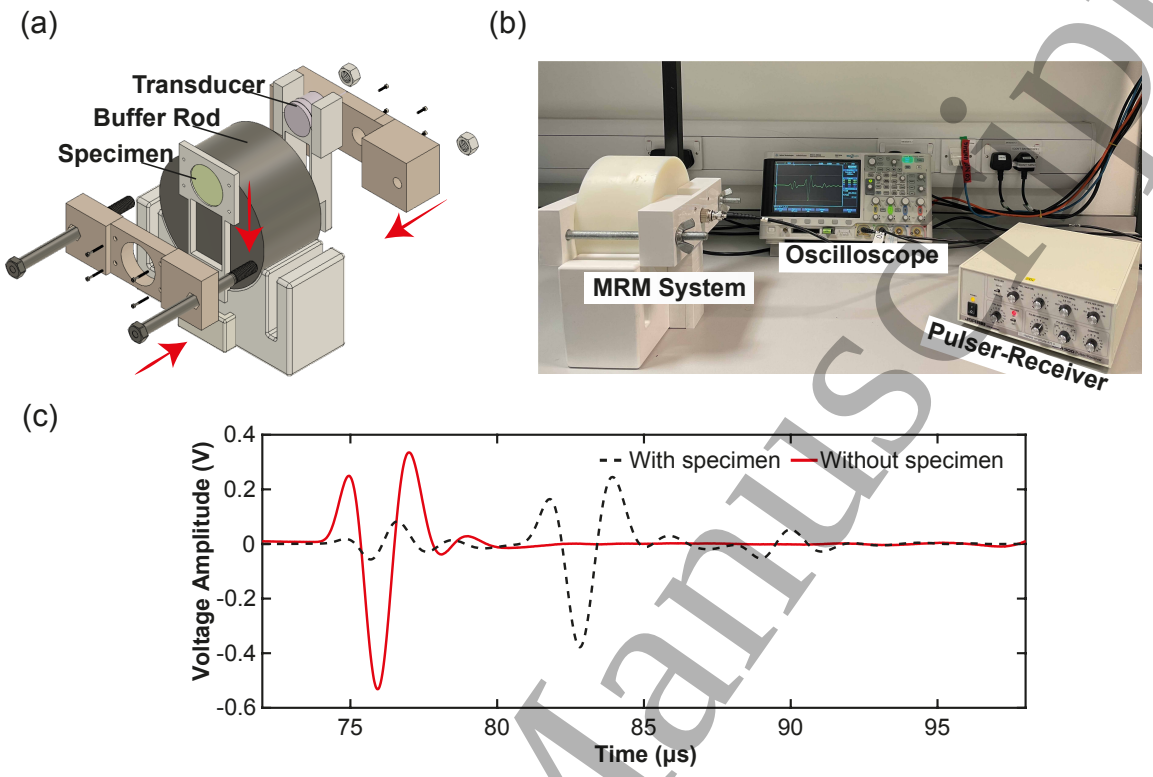

Figure 2. Evaluation Set-up of multiple-reflection method (MRM): (a) Schematics showing the experimental configuration for investigating measurement accuracy and repeatability. (b) Complete experimental apparatus comprising the MRM system interfaced with oscilloscope and pulser-receiver unit. (c) Representative paired waveform acquisitions demonstrating signal characteristics before and after specimen placement.

reaching the transducer, resulting in drive voltages of approximately 45–49 V. To ensure the absence of nonlinear propagation which may also affect measurements, the spectrum of the received signals was examined to verify that the amplitude of the second harmonic remained at least 30 dB below the amplitude of the fundamental frequency.

The recorded waveforms were processed similarly to the MRM data. The location of the peak minimum voltage was identified, and then a Tukey window with taper ratio of 0.1 was applied. Again the window started 3 μs before the temporal peak voltage and extended beyond the end of the pulse, identified by the third peak (i.e., the last positive-going half-cycle), with a window end chosen to exclude following signals. Subsequently, the single sided spectrum of the waveforms was obtained via FFT. The insertion loss, IL, in dB for each pair of specimen-reference spectra, $A_s(f)$ and $A_w(f)$ respectively was calculated by:

$$IL(f) = -20\log_{10}\left(\frac{A_s(f)}{A_w(f)}\right). \tag{13}$$

The insertion losses calculated for the two specimens $IL_{thick}(f)$ and $IL_{thin}(f)$, were then

combined to obtain frequency-dependent attenuation coefficient in units of dB/cm:

$$a(f) = \frac{IL_{thick}(f) - IL_{thin}(f)}{d_{thick} - d_{thin}} + a_w(f), \tag{14}$$

where d_{thick} and d_{thin} are the specimen thickness of the thicker and thinner specimen, respectively. $a_w(f)$ is the frequency dependent attenuation coefficient of water [42] at 20°C, obtained using the `waterAbsorption` function in the k-Wave toolbox [43]. A frequency power-law expression [44],

$$a_{fit}(f) = a_0(f)f^y, \tag{15}$$

was then fit to the measurements to obtain the power law attenuation prefactor a_0 in units of dB $\cdot$ MHz^{-y} $\cdot$ cm^{-1}, and the exponent y. f is the frequency in MHz.

For comparison with the signal velocity calculated using the MRM, signal velocity was also calculated from the SIM measurement data by

$$c(f) = \frac{d}{d/c_w - [t_w - t_s]}, \tag{16}$$

using the same three arrival-time picking criteria previously described. d is the specimen thickness in meters, c_w is the sound velocity in water at room temperature in m/s, obtained from the 5th order polynomial from Marczak [45] using the k-Wave `waterSoundSpeed` function [43]. The mean and standard deviation of the velocities were calculated from the full set of measurement data.

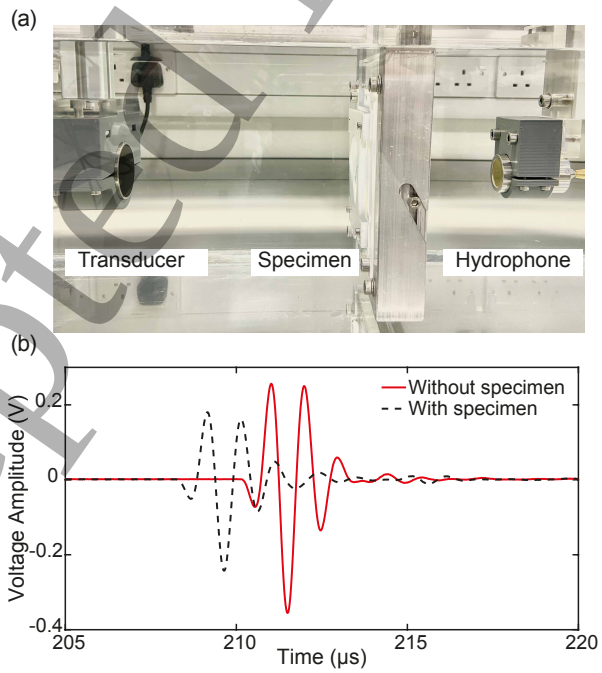

Figure 3. Reference Measurements of Through Transmission Substitution-Insertion Method (SIM): (a) Measurement set-up, with the transducer, specimen and PDVF hydrophone centrally aligned. (b) An example set of paired waveforms captured during measurement before and after specimen insertion.

2.4. Quantifying the Effect of MRM Setup on Measurements

The influence of several aspects of the experimental setup on the accuracy and precision of MRM measurements were assessed. First the effect of the compression applied to hold the system components together was examined, before effects related to the width of the buffer rod (side-wall effects), and finally the influence of the buffer rod and specimen surface roughness. Measurements under each condition were repeated five times, and compared with measurements obtained from SIM measurements.

System Compression Force Evaluation: The compression force applied to hold the system components together was adjusted using the retaining bolts. The compression was adjusted starting with loose compression and gradually tightening the bolts. It was not possible to directly measure the compression force, so the settings were quantified by measuring the distance between the specimen holder surface and the end of the bolt using a digital caliper (CD6DCX, Mitutoyo Corp., Japan). The distance was varied from 79 mm (loosest) to 83 mm (tightest) in 1 mm steps (Fig. 4a).

Buffer Rod Diameter Evaluation: To investigate the influence of buffer rod diameter, measurements were first made by making measurements with the specimen in five positions between the center and the edge of the buffer rod. The transducer position was also translated accordingly to maintain coaxial alignment of the transducer and specimen (Fig. 5a). Theoretical calculations suggest that the influence of the buffer rod on measurements in this kind of setup is minimal when its width is at least twice that of the transducer diameter for sources with radius > ten times the transducer operating wavelength [31]. The radius of the buffer rod used was 92.5 mm, while the radius of the specimen and transducer were 30.0 and 19.6 mm, respectively. The specimen was translated from the center of the buffer-rod to its edge in five 12.5 mm steps. Therefore, at the position closest to the edge of the buffer rod, the separation of the center of the transducer and the buffer rod side is 30.0 mm, which is less than twice the radius of the transducer. Since in this configuration, the distance between the edge of the buffer rod and the transducer is only reduced in one direction, additional measurements were performed using two additional buffer rods with diameters of 80.0 mm (twice the transducer diameter), and 40.0 mm (matching the transducer diameter), as illustrated in Fig. 5d.

Buffer Rod and Specimen Surface Condition Evaluation: The effect of surface roughness was examined by repeating measurements with the buffer rod and specimen surfaces polished to different levels of smoothness using the lathe as described in Sec. 2.2. The buffer rod underwent three successive polishing procedures, referred to as Level I, II and III, with each level resulting in a finer surface finish. After each polishing step, surface roughness of the buffer-rod was measured. The buffer-rod was then used for MRM measurements with each surface condition to quantify the effect of surface roughness on attenuation coefficient and sound velocity measurements.

Similarly, the impact of specimen surface roughness was evaluated following polishing, with measurements repeated under three conditions: the original surface

finished by the 3D printer, one side polished, and both sides polished. The polishing settings used for the specimen were consistent with those used for polishing the buffer rod to Level III. The thicknesses of the specimen and buffer rod were remeasured after each polishing step.

Surface roughness was quantified using a non-contact surface profilometer (Bruker DektakXT Profilometer, Germany). The measurement zone spanned 5×5 mm^2 in the center of the specimen, with 100 lines scanned laterally with 50 μm between lines and 0.55 μm step size along the lines. The vertical measurement range was 524 μm for the surface of Level I, and 65.5 μm for the surfaces of Level II and III, with the hills and valleys profile setting, 2 μm radius stylus and 3 mg stylus force. The mean surface roughness, S_a, and maximum peak height, S_p, were extracted from each measurement after correcting for the specimen tilt, according to the ISO25178-700 standard [46]. The mean surface roughness, S_a, is calculated from the arithmetic mean of absolute difference in height from the mean surface for each point. Maximum peak height, S_p, is the maximum height relative to the mean surface.

2.5. Validation of the Optimized MRM System

As a final validation of the optimized MRM system, the properties of two additional specimens - FLXA9960 and Formlabs Clear - were measured in addition to the initial RGDA8625 specimen at frequencies of 0.5 and 1.0 MHz and validated against SIM measurements. Previous measurements of these materials at frequencies of 1.0 MHz and above showed that their attenuation coefficients differ significantly from RGDA8625, providing a range of values for validation of the system [35]. The FLXA9960 specimen was fabricated as the RGDA8625 specimen with a 60 mm diameter, and thicknesses of 4 and 8 mm. Both specimens were used in SIM measurements, only the 8 mm specimen was used in MRM measurements. The Formlabs Clear specimen was fabricated with a diameter of 60 mm, and thicknesses of 8 and 12 mm. The specimen with 12 mm thickness was used in MRM measurements. The increased thickness of the Formlabs Clear specimen was required to enable separation of echoes given its higher sound velocity [35].

The MRM measurements were conducted using the system parameters determined to be optimal in this study. For the 1.0 MHz measurement, a single-element planar transducer with a diameter of 39.1 mm (V389, Panametrics-NDTTM, Olympus NDT, Waltham, MA, USA) served as both transmitter and receiver. The same transducer was used for the SIM measurements, where the pulse voltage amplitudes were set at 40 and 45 mV, with the same transmitter-receiver distances as those used in 0.5 MHz SIM measurement. After amplification, these settings corresponded to drive voltages of approximately 17.9 and 20.1 V, respectively. The signal processing and calculation procedures were as described in Section 2.2, and 2.3.

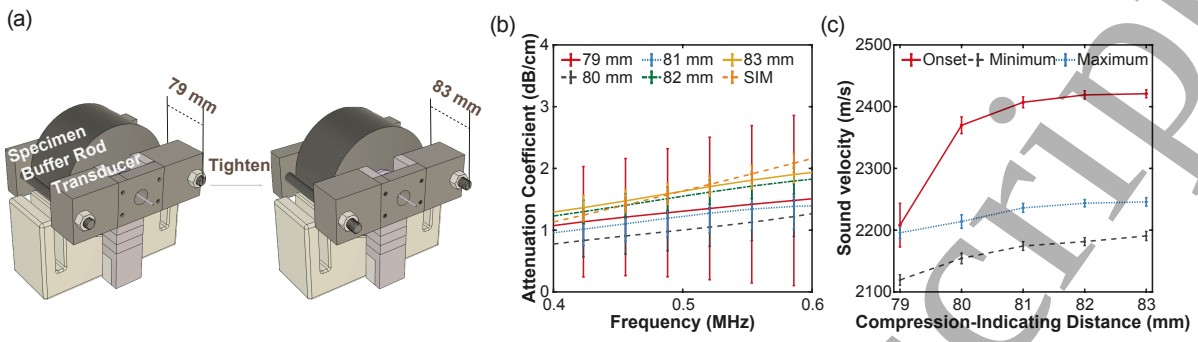

Figure 4. System Compression Evaluation: (a) Diagram illustrating the effect of compression on the multiple-reflection method (MRM) measurement system, achieved by tightening the retaining bolts which increased the distance between the specimen holder surface and bolt end from 79 to 83 mm in 1 mm increments. (b) The attenuation coefficient of RGDA8625 material measured under varied compression levels (indicated by distances from 79 to 83 mm) compared with substitution-insertion method (SIM) reference measurements. (c) Sound velocities calculated via Time-of-Flight (TOF) using three time picking criteria: waveform onset, minimum value, and maximum value. Error bars in (b, c) represent standard deviations from: MRM measurements (n=5) and SIM measurements (n=4).

3. Results

3.1. System Compression Force

Measurement accuracy and repeatability was found to improve as system compression was increased. The attenuation coefficient curves converged towards the reference SIM curve (Fig. 4b) as the system was tightened. The attenuation coefficient at 0.5 MHz ranged from 1.3 ± 1.1 dB/cm in the worst case to 1.7 ± 0.2 dB/cm for the tightest setting, in agreement with the SIM value of 1.6 ± 0.1 dB/cm. Further tightening caused no further change. In addition, the standard deviation of the attenuation coefficient at 0.5 MHz decreased from 1.09 dB/cm at the loosest 79 mm setting, to 0.19 at the 82 mm setting then to 0.16 dB/cm at the tightest 83 mm setting. It was also observed that the sound velocities converged to a stable value once the system was tightened to the 82 mm setting, for example, increasing from 2269 ± 20 m/s to 2421 ± 6 m/s when arrival time was derived from waveform onset.

Regarding the measured sound velocities, regardless of the time-picking criteria applied, all calculated velocities showed a similar increasing trend with system tightening (Fig. 4c). The sound velocities calculated using onset waveform criteria were consistently higher than those obtained using peak negative and positive waveform criteria across all compressional force settings. Further comparison of velocities calculated by MRM and SIM is further analysed in Sec. 3.5. Based on these observations, the 82 mm setting was established as the minimum compression setting for use in subsequent measurements to establish the effect of the other experimental factors.

3.2. Buffer Rod Diameter

In the first set of measurements, buffer side wall effects were investigated by translating the specimen and transducer from the center of the 185 mm diameter buffer rod towards the edge. At the central position, the measured attenuation coefficient at 0.5 MHz was 1.7 ± 0.2 dB/cm, which agreed with the reference SIM measurement of 1.6 ± 0.1 dB/cm to within the standard deviation. However, as the transducer and specimen were moved towards the edge, the measured attenuation coefficient decreased to 0.5 ± 0.2 dB/cm (Fig. 5b). With this positional shift, the standard deviation of the attenuation coefficient also increased from 0.16 dB/cm to 0.21 dB/cm, indicating reduced measurement repeatability. Further, the frequency dependence of the attenuation coefficient obtained at the edge position deviated from the expected trend of increasing attenuation with frequency [12]. In contrast, the sound velocities calculated using each time-picking criteria remained stable during specimen and transducer repositioning (Fig. 5c). The maximum velocity variation was less than 1%. For instance, the sound velocity determined from the waveform onset changed from 2429 ± 8 m/s in the third positioning to 2407 ± 7 m/s at the edge position. The sound velocities calculated using the waveform onset time-picking criteria consistently yielded higher values compared to the other two criteria across all specimen and transducer positions, a pattern consistent with the previous investigation of system compressional force.

In the second set of measurements, we employed three different buffer rod diameters to further investigate edge effects , maintaining the same side wall distance in all directions. The attenuation coefficients measured with the larger buffer rods (185 mm and 80 mm in diameter) were 1.7 ± 0.2 dB/cm and 1.6 ± 0.1 dB/cm respectively at 0.5 MHz, agreeing closely with the SIM measurement of 1.6 ± 0.1 dB/cm. However, with the smallest buffer rod (40 mm in diameter), which was comparable in size to the transducer, the attenuation coefficient was significantly lower across the measured frequency range, with a value of 0.9 ± 0.1 dB/cm at 0.5 MHz, a 44% decrease (Fig. 5e). This difference may be attributed to enhanced boundary reflections and consequently stronger interference between echoes due to the narrower buffer rod. This interference is evident in the comparison of waveforms reflected at the buffer rod-air interface, where the waveforms obtained with the 40 mm diameter buffer rod differed in shape significantly from those obtained with the two larger buffer rods (Fig. 5f). Based on our findings, the buffer rod diameter in this MRM system should be at least twice the transducer diameter to mitigate side-wall effects on measurement accuracy and precision. The 185 mm diameter buffer rod was selected for subsequent investigation of surface roughness effects.

3.3. Buffer Rod Surface Condition Evaluation

The buffer rod surface was sequentially polished to three increasingly smooth finishes (Level I, II and III). Surface profiles of each surface finish are presented in Fig. 6 a-c, with their corresponding mean surface roughness (S_a) and maximum peak height

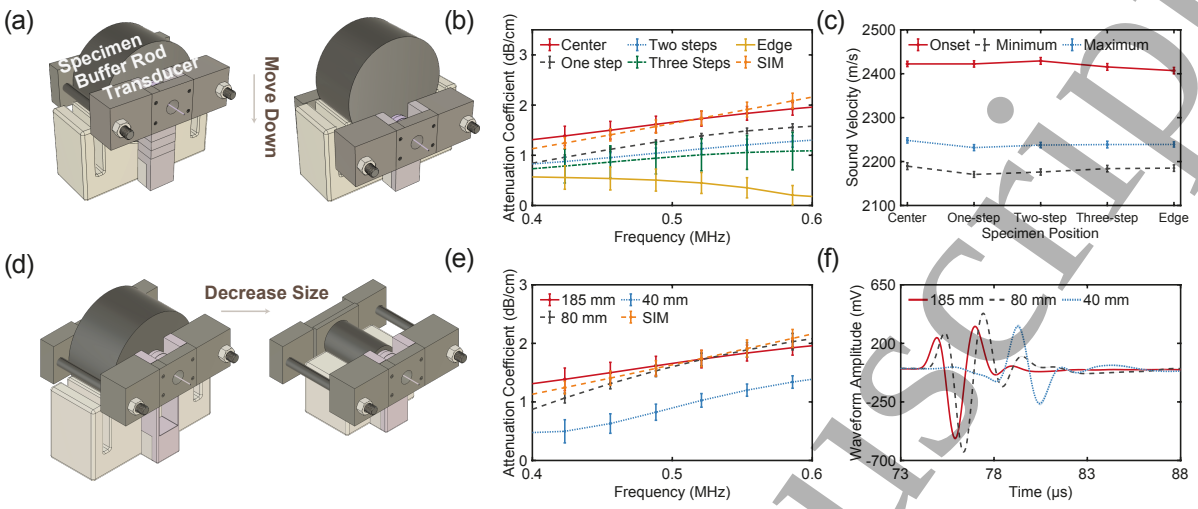

Figure 5. Buffer Rod Diameter Evaluation: (a) Diagram illustrating translation of the coaxially aligned transducer and specimen from the center to the edge of the buffer rod for multiple-reflection method (MRM) measurement. (b) The attenuation coefficient of RGDA8625 material measured at different radial positions from center to edge of the buffer rod (center, one step, two steps, three steps, and edge corresponding to distances of 0, 23.1, 46.2, 69.3, and 92.5 mm respectively between specimen center and buffer rod center), compared with substitution-insertion method (SIM) reference measurements. (c) Sound velocities calculated via Time-of-Flight (TOF) using three time picking criteria: waveform onset, minimum value, and maximum value. (d) Schematics showing changes in the buffer rod diameter and assembly set-up with three buffer rod diameters (185 mm, 80 mm, and 40 mm). (e) The attenuation coefficient of RGDA8625 material measured using each buffer rod diameter (185, 80, and 40 mm), compared with SIM reference measurements. (f) The reflected waveform at the buffer rod-air interface measured for each buffer rod diameter. Error bars in (b, c and e) represent standard deviations from: MRM measurements (n=5) and SIM measurements (n=4).

(S_p) values detailed in Table 1. The buffer rod surfaces was smooth compared to the wavelength for all finishes. For level I, the wavelength-to-S_a ratio exceeded 2700, and the wavelength-to-S_p ratio was greater than 150. At Level III, these ratios increased significantly, to 5800 for wavelength-to-S_a ratio and 1052 for wavelength-to-S_p ratio.

The attenuation coefficient measured using the Level I buffer rod surface finish of 1.7 ± 0.2 dB/cm aligned closely with SIM reference measurement of 1.6 ± 0.1 dB/cm at 0.5 MHz (Fig. 6d). The buffer rod was polished initially to level I on manufacture, for which there was good agreement with SIM measurements. Further polishing to level II did not change the S_a greatly but did reduce the S_p level. However, further polishing of the buffer rod surface resulted in lower attenuation coefficient with a larger difference from the reference SIM measurements. At Level II and III, the attenuation coefficients at 0.5 MHz were 1.34 ± 0.07 dB/cm and 1.39 ± 0.11 dB/cm respectively.

The attenuation coefficients were calculated using reflection coefficients R_{12} at the buffer rod-to-specimen interface calculated using measurements from Eq. 9 rather than the theoretical value. The measured R_{12} at 0.5 MHz was 0.22, 0.28 and 0.26 for Level

Table 1. Buffer Rod Surface Condition Evaluation.

Level	S_a (μm)	S_p (μm)	λ / S_a	λ / S_p
Level I	1.59	24.90	2965	189
Level II	1.69	14.00	2789	337
Level III	0.80	4.48	5893	1052

S_a = Mean surface roughness, S_p = Maximum peak height, λ, the wavelength of sound in the Nylon 6.6 buffer rod, was 4.7 mm at 0.5 MHz with a sound velocity of 2357 m/s.

I to III buffer rod surfaces respectively, all increasing with frequency (Fig. 6e). These measured R_{12} values ($\sim$0.2) remain substantially higher than the theoretical R_{12} of 0.04 $\pm$ 0.04 (k = 1).

The theoretical value was calculated using following acoustic properties: sound velocities of 2357 $\pm$ 118 m/s (buffer rod, measured in-house) and 2457 $\pm$ 123 m/s (specimen) [35], and densities of 1138 $\pm$ 25 kg/m^3 (buffer rod, measured in-house) and 1175 $\pm$ 26 kg/m^3 (specimen) [35].

We estimated random uncertainty in sound velocity at $\sim$5% by combining in quadrature [47] the $\sim$1% uncertainty in specimen thickness with standard deviation of velocity measurements. Mean sound velocity from six measurements (three time-picking criteria, two methods) had standard deviation of $\sim$4-5% . Similarly, we estimated uncertainty in specimen density to be $\sim$2.2% by combining $\sim$1% mass measurement uncertainty with $\sim$2% uncertainty in volume derived from specimen dimensions. These uncertainties represent random errors only and likely underestimate the total measurement uncertainty. Additionally, the measured reflection coefficients showed an increasing trend with frequency.

The differences in velocities calculated using the three time-picking criteria diminished as the buffer rod surface roughness decreased from Level I to III. The velocity calculated from the temporal peak negative and positive voltages decreased by 35 m/s (1.6%) from 2190 $\pm$ 8 m/s to 2155 $\pm$ 6 m/s, and 47 m/s (2.1%) from 2248 $\pm$ 6 m/s to 2201 $\pm$ 9 m/s, respectively, while the velocity calculated from waveform onset showed a more substantial decrease of 204 m/s (8.4%) from 2422 $\pm$ 6 m/s to 2218 $\pm$ 7 m/s (Fig. 6f). The significant velocity reduction observed using the waveform onset criterion demonstrated its sensitivity to buffer rod surface changes compared to the other two time-picking methods. Moreover, the velocities measured by all three time-picking criteria converged as buffer rod surface was smoothed from Level I to III.

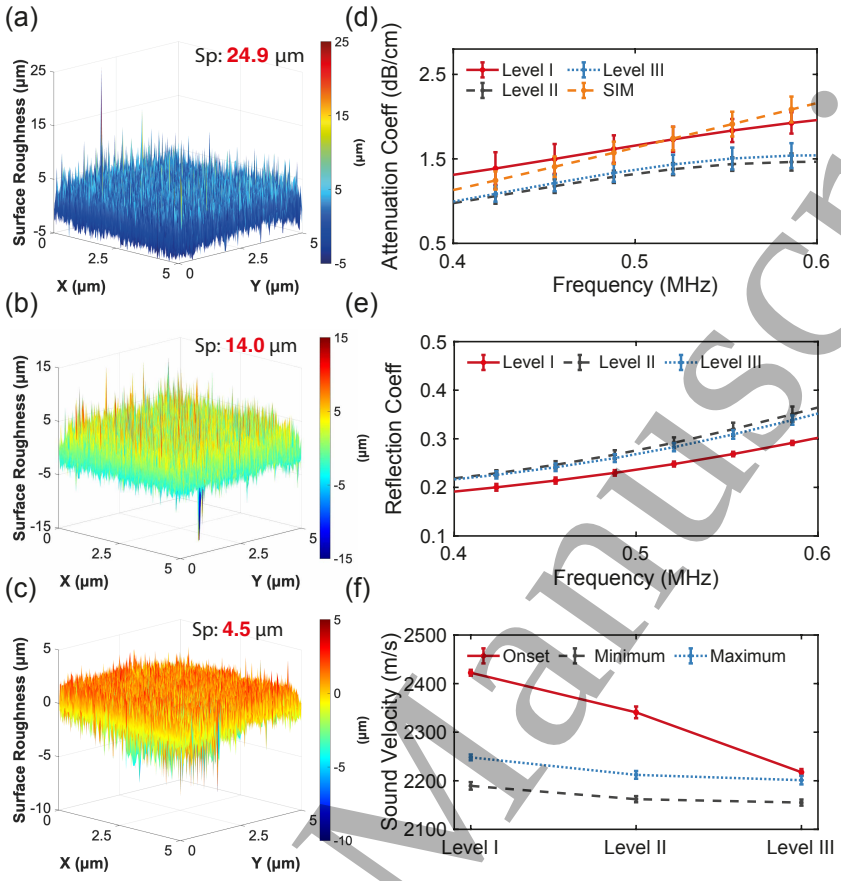

Figure 6. Buffer Rod Surface Condition Evaluation: (a-c) The buffer rod surface profile at three progressive polishing levels I to III, with S_p values indicating the corresponding maximum peak height. (d) The attenuation coefficient of RGDA8625 material derived from multiple-reflection method (MRM) under three buffer rod surface level conditions, compared with substitution-insertion method (SIM) reference measurements. (e) The reflection coefficients at the buffer rod to RGDA8625 interface under three buffer rod surface level conditions. (f) Sound velocities calculated via Time-of-Flight (TOF) using three time picking criteria: waveform onset, minimum value, and maximum value under three buffer rod surface level conditions. Error bars in (d-f) represent standard deviations from: MRM measurements (n=5) and SIM measurements (n=4).

3.4. Specimen Surface Condition Evaluation

The influence of specimen surface polishing on attenuation coefficient and sound velocities was evaluated by comparing measurements made on the unpolished RGDA8625 specimen and with one or both sides polished against SIM reference measurements. The MRM and SIM derived attenuation coefficients for the unpolished and two-side polished specimens exhibited good agreement in general. However, for the unpolished specimen, the frequency dependence of the MRM derived attenuation coefficient differed from the SIM measurement, and began to decrease with frequency above approximately 0.6 MHz, as shown in Fig. 7a. The MRM derived attenuation coefficients measured for the specimen with one side polished differed from those

Table 2. Specimen Surface Roughness

Level	S_a (μm)	S_p (μm)	λ / S_a	λ / S_p
Original	2.16	9.75	2275	504
Polished	0.26	0.34	18900	1445

S_a = arithmetical mean height, S_p = maximum peak height, λ, the Wavelength of sound in RGDA8625, was 4.9 mm at 0.5 MHz with a sound velocity of 2457 m/s.

measured using SIM, regardless of the orientation of the polished surface relative to the transducer (Fig. 7b).

For further comparison, the attenuation coefficients measured for each specimen surface condition using MRM and SIM respectively are plotted in Fig. 7d and e. The MRM-derived attenuation coefficients increased as the specimen was polished on first one side then the other from 1.47 ± 0.12 dB/cm, to 2.01 ± 0.17 dB/cm, then 2.18 ± 0.18 dB/cm at 0.5 MHz. This change may have been influenced by the slight reduction in thickness of the specimen after polishing, which resulted in narrower separation between echoes from the specimen top and bottom. Further, the surface conditions had a more pronounced effect on SIM measurements compared to their influence on MRM measurements. The maximum change in mean attenuation coefficient at 0.5 MHz was 0.71 dB/cm for MRM measurements versus 1.09 dB/cm for SIM, with the latter mainly due to measurements from the single-side polished specimen.

The velocities were consistent across all three time-picking methods (waveform onset, peak negative and positive) for both the unpolished and two-side polished specimen (Fig. 7f). However, the single-side polished specimen showed notably lower velocities. For example, using the waveform peak positive method, the velocities were 2155 ± 6 m/s for the unpolished specimen surfaces, declining to 2016 ± 9 m/s with the single-side polished, and returning to 2144 ± 14 m/s after polishing both sides. The similarity in velocities measured for the unpolished and two-side polished specimen may be attributed to the condition of the surface, for which the wavelength-to-S_a ratios exceed 2000 (Table 2). The lower velocities in the single-side polished specimen may result from complex wave reflection and effects due to the difference in the specimen interfaces.

3.5. Validation of the Optimised MRM System

To validate the system after initial optimisation with RGDA8625 at 0.5 MHz, additional measurements were conducted on RGDA8625 at 1.0 MHz with both sides polished, and on two more 3D printing materials, Formlabs Clear and FLXA9960, each tested at both 0.5 and 1.0 MHz (Fig. 8). At 1.0 MHz, the MRM-derived attenuation coefficient of RGDA8625 was 3.60 ± 0.36 dB/cm, differing by 7.5% from the SIM measurement of 3.88 ± 0.17 dB/cm. This difference was similar to the 7.8% difference observed at 0.5

MHz, where MRM and SIM measurements were 2.10 ± 0.19 dB/cm and 2.27 ± 0.16 dB/cm, respectively.

The MRM measurements made on both the Formlabs Clear and FLXA9960 specimens, the attenuation coefficients of which were similar to or higher than the RGDA8625 material, agreed reasonably well with reference SIM measurements at both frequencies. For Formlabs Clear at 0.5 MHz, the MRM-derived attenuation coefficient was 1.61 ± 0.11 dB/cm, compared with the SIM-derived value of 2.06 ± 0.45 dB/cm (Fig. 8c). At 1.0 MHz, the MRM and SIM measurements yielded attenuation coefficients of 3.42 ± 0.16 dB/cm and 3.64 ± 0.13 dB/cm respectively, a difference of 6.2% (Fig. 8d). The FLXA9960 specimen had a higher attenuation coefficient, the MRM-derived value was 4.7 ± 0.5 dB/cm at 0.5 MHz compared to the SIM value of 5.6 ± 0.7 dB/cm (Fig. 8e), and 11.8 ± 1.5 dB/cm at 1.0 MHz compared to the SIM value of 11.1 ± 0.7

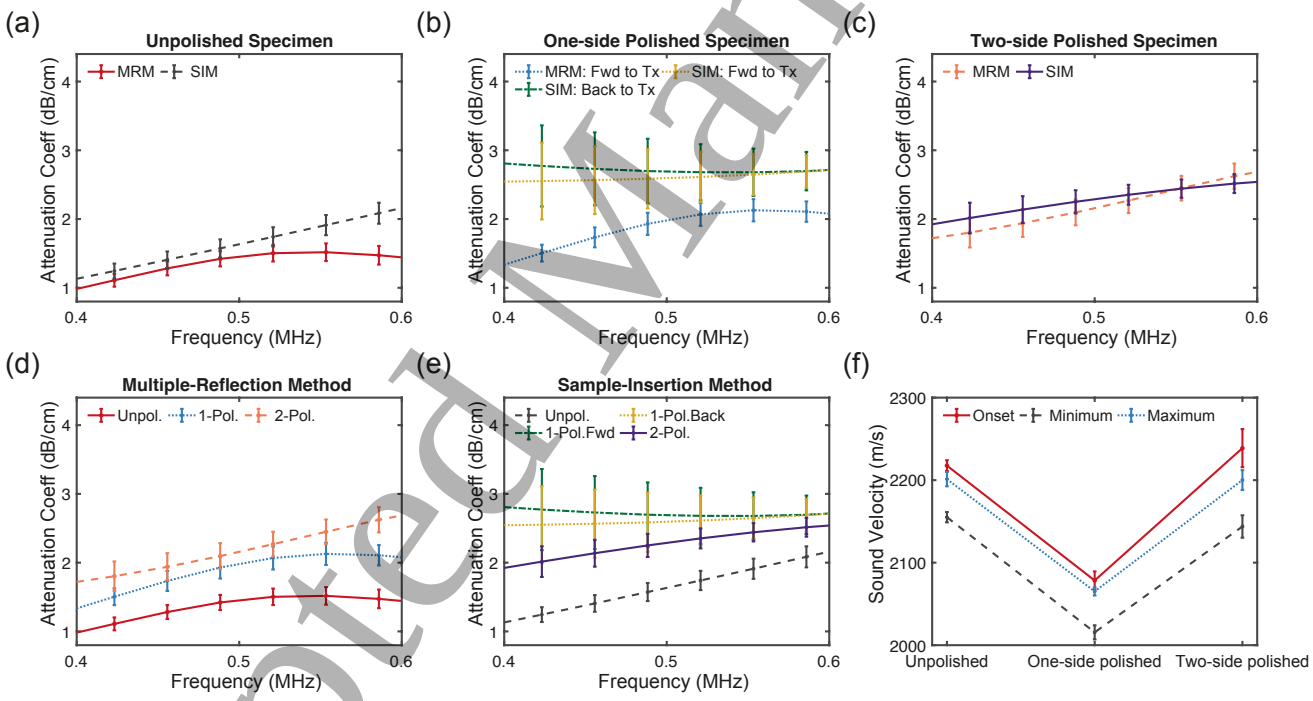

Figure 7. Specimen Surface Condition Evaluation: The attenuation coefficient of RGDA8625 material measured under three specimen surface conditions: (a) unpolished specimen, (b) single-side polished specimen with orientations relative to the transmitter (Tx) indicated as 'Fwd' (forward-facing) and 'Back' (backward-facing), and (c) double-side polished specimen, derived from multiple-reflection method (MRM) and compared with substitution-insertion method (SIM) reference measurements. (d) MRM measurements made with each specimen surface condition, and (e) SIM measurements made with each specimen surface condition. Legend abbreviations: Unpol. = unpolished, 1-Pol.Fwd/Back = single-side polished with polished surface facing forward/backward relative to transmitter, 2-Pol. = double-side polished. (f) Sound velocities calculated via Time-of-Flight (TOF) using three time picking criteria: waveform onset, minimum value, and maximum value under three specimen surface conditions. Error bars in (a-f) represent standard deviations from: MRM measurements (n=5) and SIM measurements (n=4).

dB/cm (Fig. 8f).

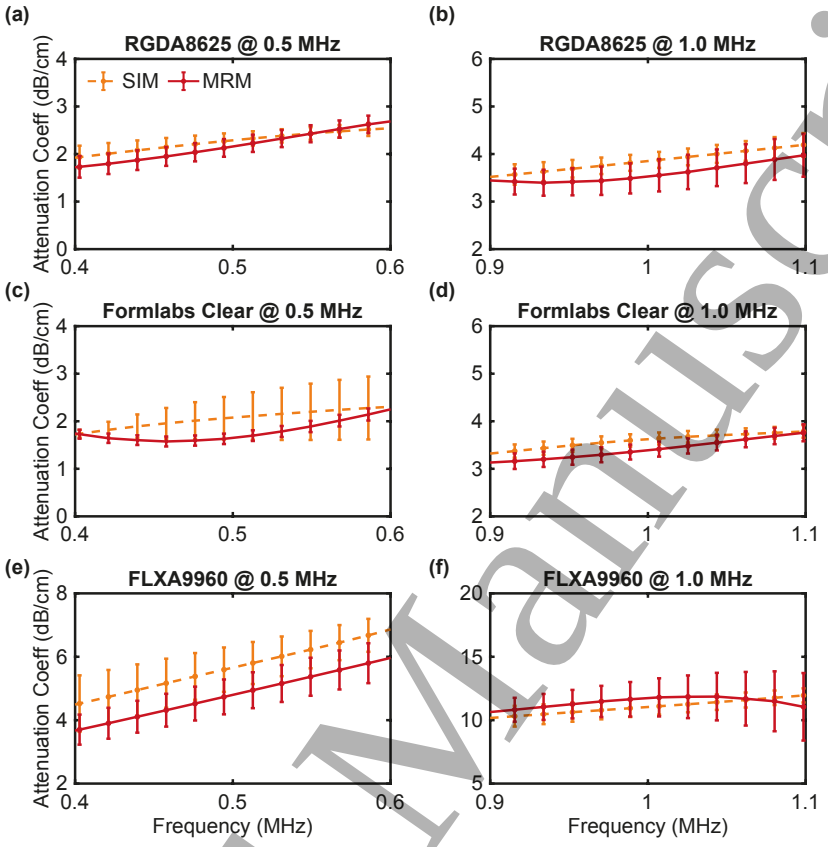

Figure 8. Validation of the Optimised MRM System: Attenuation coefficients of RGDA8625 material at (a) 0.5 MHz, (b) 1 MHz, and FLXA9960 material at (c) 0.5 MHz, (d) 1 MHz, and Formlabs Clear material at (e) 0.5 MHz and (f) 1 MHz, measured using both multiple-reflection method (MRM, solid red line) and substitution-insertion method (SIM, dashed orange line). A single shared legend is positioned at panel (a). Error bars in (a-f) represent standard deviations from: MRM measurements (n=5) and SIM measurements (n=4).

The sound velocities of the three specimens measured by both MRM and SIM, using the three time-picking criteria (waveform onset, temporal peak positive and negative voltage) are presented in Table 3. There were differences in the velocities measured using MRM and SIM of between 7.0% and 12.5%, which were more pronounced than the differences arising from the use of different time-picking criteria within each method (maximum 5.2%). This suggests that the choice of measurement method has a greater impact on velocity determination than the selection of time-picking criteria within a single method. Additionally, while the difference in velocity arising from the choice of time-picking criteria are greater than the standard deviation of the measurements (maximum 1.7% via MRM and 2.7% via SIM), these variations suggest time-picking criteria contribute 3-5% to the overall measurement uncertainty.

Table 3. Sound Velocity Calculated Using Time-of-Flight Method from MRM and SIM Measurements

Specimen	FLXA9960	RGDA8625	Formlabs Clear
Sound velocity (m/s) @ waveform **onset**	**MRM: 1815 ± 15** SIM: 1953 ± 10 Difference: 8.7%	**2230 ± 7** 2365 ± 27 Difference: 7.3%	**2346 ± 7** 2565 ± 13 Difference: 9.7%
Sound velocity (m/s) @ waveform **peak positive** voltage	**MRM: 1750 ± 13** SIM: 1954 ± 14 Difference: 12.5%	**2155 ± 6** 2341 ± 32 Difference: 9.9%	**2350 ± 7** 2559 ± 17 Difference: 9.5%
Sound velocity (m/s) @ waveform **peak negative** voltage	**MRM: 1793 ± 13** SIM: 1933 ± 14 Difference: 9.0%	**2201 ± 9** 2377 ± 32 Difference: 9.4%	**2390 ± 6** 2561 ± 15 Difference: 7.7%
Maximum difference between time-picking criteria	**MRM: 5.2%** SIM: 2.5%	**4.0%** 4.2%	**2.4%** 1.4%

The standard deviation for MRM measurements was calculated from five repeated measurements, and for SIM measurements were measured under two transducer-to-hydrophone distances, and with two pulse voltage amplitudes.

4. Discussion

We optimised the multiple-reflection method (MRM) setup through experimentally quantifying the influence of system compressional force, and buffer rod side-wall effects, and examining the effect of buffer rod and specimen surface roughness. Our findings demonstrate that reliable MRM measurements require adequate compression. In our setup, this compression serves a similar purpose to the pressure applied in clinical ultrasound imaging [48]: it ensures good contact between the transducer, buffer rod (Nylon 6.6), and the test specimen by minimising interfacial air gaps, reducing couplant layer thickness, preventing uneven couplant distribution, maintaining uniform contact pressure, avoiding component misalignment, and preventing partial contact loss. Adequate compression can be achieved through robust mechanical design that securely stabilises the transducer, buffer rod, and specimen relative to one another. The designed mechanical assembly can be verified using a convergence test before measurement, as our experiments showed that attenuation coefficients and sound velocities converge once sufficient compression is applied.

Additionally, for sources such as the one used here, which is large relative to the wavelength at the operating frequency, the buffer rod diameter should be at least twice the size of the transducer in order to effectively minimise boundary reflection interference in the measurement. Using a buffer rod the same size of the transducer resulted in a 40% deviation in the attenuation coefficient of RGDA8625 at 0.5 MHz compared to the SIM reference test.

The reflection coefficient at the buffer rod-specimen interface R_{12} is needed to calculate the specimen's attenuation coefficient using Eq. 9 by MRM measurement. Our results indicate that both the buffer rod and specimen surfaces require consistent flatness and surface smoothness on both sides for MRM measurements. Similarly,

the importance of consistently polishing both sides of the specimen surface for SIM attenuation coefficient measurement is highlighted in Fig. 7e. The surface condition can be evaluated through surface quantification by profilometer measurement [49]. The comparison between the surface roughness and the measurement wavelength may serve as an important indicator to justify whether the buffer rod and specimen smoothness are sufficient for use in MRM measurement. Alternatively, adequate buffer rod surface conditioning can be verified by convergence in measured sound velocities in the specimen with different arrival time-picking methods (onset, negative and positive peak of waveform). In Fig. 6f, the sound velocities calculated using three time-picking methods are shown to converge at the Level III buffer rod surface finish, suggesting optimal buffer rod surface conditioning for MRM measurement.

Additionally, the measured R_{12} should be used for attenuation coefficient measurement in MRM. Our experiments revealed significant discrepancies between theoretical and measured R_{12} values. While theory predicted $R_{12} = 0.04$, experimental measurements across three buffer rod surface smoothness levels showed values between 0.2 and 0.3. Similar disparities were observed at the fused quartz buffer rod and nickel 200 specimen interface, where the measured R_{12} was 0.9 at 100 MHz compared to the theoretical value of 0.5 [32]. Furthermore, our measurements and previous studies [32] showed that measured R_{12} values fluctuated across frequencies, unlike the frequency-independent theoretical R_{12} calculated using 8. These substantial differences between measured and theoretical R_{12} values could significantly affect attenuation coefficient measurements. Since attenuation coefficients should be independent of buffer rod and specimen surface conditions, using an experimentally measured R_{12} value is essential for accurate MRM measurements.

The discrepancy between the theoretical R_{12} (maximum value of $\sim$0.08) and measured values ($\sim$0.2) may arise from the fact that the estimated uncertainties only represent random errors, meaning the total measurement uncertainty is likely underestimated. Further systematic effects may arise for example from deviations from ideal plane-wave conditions and thin coupling layers not accounted for in the theoretical model.

Regarding the increase in measured reflection coefficient with frequency, the calculation uses echoes from both the buffer rod-air interface (where $R_{air} \approx 1$) and the buffer rod-specimen interface. The buffer rod-air interface produces echoes with longer trailing oscillations compared to the buffer rod-specimen interface. Through Fourier analysis, these extended oscillations create a spectrum that peaks at lower frequencies, contributing to the observed frequency-dependent behaviour. The amplitude of these oscillations may be below the noise floor in the signal returned from the buffer rod-specimen interface.

The MRM optimisation described here was performed on a specimen of RGDA8625 at 0.5 MHz, before verification with two additional materials, Formlabs Clear and FLXA9960, at both 0.5 and 1.0 MHz. Good agreement between these MRM measurements against benchmark SIM measurements established the applicability of

this MRM system under other conditions.

We further compared our MRM attenuation measurement results with the published SIM data from identical 3D printed specimens [35]. The previous measurements used a 2.25 MHz center frequency transducer which had a bandwidth of 1-3 MHz, allowing comparison of attenuation coefficients at 1 MHz. For the Formlabs Clear specimen, the MRM-measured attenuation coefficient at 1.0 MHz was 3.42 ± 0.16 dB/cm, differing by 13.4% from the previous SIM measurement of 2.99 ± 0.39 dB/cm. For the FLXA9960 specimen, the MRM-derived attenuation coefficient was 11.83 ± 1.54 dB/cm, higher than the published SIM results of 7.99 ± 0.48 dB/cm. For both materials, the differences between our MRM-derived values and the previous SIM measurement were larger than those between our self-employed MRM and SIM measurements. This discrepancy may be due to the different bandwidths of the two sources. The published SIM measurement [35] used a 2.25 MHz center frequency transducer, with the 1 MHz data at the lower limit of the measurement bandwidth resulting in a reduced signal-to-noise ratio [50]. In contrast, our study used a 1 MHz center frequency transducer for both MRM and SIM measurements, ensuring good SNR in both cases.

Comparing our SIM measurement with the previous paper [35], the differences in sound velocity were 7.6% (2108 and 1953 m/s), 5.6% (2502 and 2365 m/s), and 2.4% (2629 and 2565 m/s) for FLXA9960, RGDA8625, and Formlabs Clear, respectively, using waveform onset for arrival time detection. These differences correlate with material attenuation coefficient (FLXA9960 > RGDA8625 > Formlabs Clear): more highly attenuating materials showed larger discrepancies in the SIM-measured sound velocities between studies. This correlation likely occurs because higher attenuation causes greater waveform distortion and amplitude reduction [51], affecting the accuracy of waveform onset and peak time-arrival detection. This phenomenon also explains the significant differences we observed between the MRM and SIM sound velocity measurements. The largest discrepancy was 12.5% when using the waveform peak positive time-picking method (Table 3). This larger difference may arise due to attenuation in the Nylon 6.6 buffer rod (2.7 dB/cm [52]) which is far greater that for the water propagation path (0.0017 dB/cm [42]) in SIM, causing greater waveform distortion and amplitude loss.

The comparison of sound velocity between MRM and SIM reveals that time-picking criteria account for up to 5.2% of the observed difference, while the overall discrepancy between methods ranges from 7.0 to 12.5% (Table 3). This remaining discrepancy likely stems from systematic, method-dependent factors.

For SIM, precise alignment is critical, while MRM measurements are additionally influenced by coupling conditions and signal-to-noise ratio. Furthermore, both methods employ large-area phase-sensitive sensors, which can introduce measurement errors when wavefront distortion occurs—if the wavefront is not perfectly planar across the sensor surface, different regions detect different phases, leading to phase averaging errors. Additionally, the differences in propagation path between MRM and SIM setups may affect the measurements. In MRM measurements, the echoes are more significantly attenuated, causing greater changes in shape which can affect time picking. These

method-specific systematic uncertainties, rather than random variations, account for the observed differences between SIM and MRM measurements. Furthermore, while SIM enables phase velocity calculations by comparing waveforms propagated in water with and without specimen insertion, this phase-unwrapping approach cannot be extended to MRM due to complicated phase changes from reflections at solid-air and solid-solid interfaces [53, 54], making phase-based velocity calculations currently inapplicable.

To ensure the accuracy of our longitudinal wave measurements, we must evaluate the potential influence of shear waves in our experimental configuration. In our MRM setup, the transducer positioned on the cylinder buffer rod generates longitudinal waves efficiently at normal incidence. Efficient shear wave generation requires oblique incidence or specialized transducers (e.g., wedge-based, angle-beam) [55]. The ultrasound beam is not very divergent, and the chosen buffer rod diameter is large enough to avoid reflections from the side walls. Together with the flat, tightly coupled interfaces, this minimizes energy leakage into shear modes. Any shear components generated, for example by edge waves from the transducer, will be weakened due to high shear attenuation, and are unlikely to be temporally coincident due to the shear wave velocity. Shear wave velocities are much lower than longitudinal velocities: while specific shear wave velocity data for Nylon 6.6 was not available in literature, a similar polyamides P$A_1$2 has a shear velocity of 974.7 m/s [56], significantly lower than the longitudinal velocity in Nylon 6.6 of 2457 m/s. Additionally, polymer materials typically exhibit attenuation coefficients approximately three times higher for shear waves than for longitudinal waves [57]. Given these factors, the influence of shear waves on these measurements of longitudinal velocity and attenuation coefficient is negligible.

5. Conclusion

The multiple-reflection method (MRM) enables acoustic measurements under extreme conditions, but requires optimisation of key experimental parameters. We experimentally investigated the effect of system compression, buffer rod diameter, and surface condition on measurements of attenuation coefficient and sound velocity, using the substitution-insertion method (SIM) as a benchmark. Our findings established three critical requirements: sufficient system compression (verified by experimental convergence), a buffer rod diameter at least twice the transducer diameter to minimize side-wall effects, and well-polished surfaces with average roughness smaller than the wavelength. These parameters were validated for three materials at both 0.5 and 1.0 MHz. This investigation of MRM optimisation supports the use of MRM as a complementary method to SIM at ambient temperature for validation, or as a technique for accurate and repeatable acoustic measurements under extreme conditions.

Acknowledgments

This work was supported in part by a UK Research and Innovation (UKRI) Future Leaders Fellowship (Grant No. MR/T019166/1) and by EPSRC Center for Doctoral Training (CDT) in Intelligent, Integrated Imaging In Healthcare (i4health)(EP/S021930/1). The authors would like to acknowledge Simon Hemsley from the Department of Space and Climate Physics, University College London (UCL), for his assistance with buffer rod and specimen polishing. For the purpose of open access, the author has applied a Creative Commons Attribution (CC BY) license to any Author Accepted Manuscript version arising.

References

[1] T. Meures, L. Paul, M. Ribordy, IceCube Collaboration, et al. Research and calibration of acoustic sensors in ice within the spats (south pole acoustic test setup) project. *Nucl. Instrum. Methods Phys. Res. A*, 662:S230–S233, 2012.

[2] T. G. Leighton and P. R. White. Quantification of undersea gas leaks from carbon capture and storage facilities, from pipelines and from methane seeps, by their acoustic emissions. *Proc. R. Soc. A Math. Phys. Eng. Sci.*, 468(2138):485–510, 2012.

[3] S. Zhang, G. Shen, L. An, and Y. Niu. Online monitoring of the two-dimensional temperature field in a boiler furnace based on acoustic computed tomography. *Appl. Therm. Eng.*, 75:958–966, 2015.

[4] M. Murakami, Y. Ohishi, N. Hirao, and K. Hirose. A perovskitic lower mantle inferred from high-pressure, high-temperature sound velocity data. *Nature*, 485(7396):90–94, 2012.

[5] W. T. Shi, F. Forsberg, A. L. Hall, R. Y. Chiao, J.-B. Liu, S. Miller, K. E. Thomenius, M. A. Wheatley, and B. B. Goldberg. Subharmonic imaging with microbubble contrast agents: Initial results. *Ultrason. Imaging*, 21(2):79–94, 1999.

[6] F. Forsberg, J.-B. Liu, W. T. Shi, J. Furuse, M. Shimizu, and B. B. Goldberg. In vivo pressure estimation using subharmonic contrast microbubble signals: Proof of concept. *IEEE Trans. Ultrason. Ferroelectr. Freq. Control*, 52(4):581–583, 2005.

[7] K. Kalayeh, J. B. Fowlkes, A. Chen, S. Yeras, M. L. Fabiilli, J. Claflin, S. Daignault-Newton, W. W. Schultz, and B. S. Sack. Pressure measurement in a bladder phantom using contrast-enhanced ultrasonography—a path to a catheter-free voiding cystometrogram. *Invest. Radiol.*, 58(3):181–189, 2023.

[8] K. Kalayeh, J. B. Fowlkes, J. Claflin, M. L. Fabiilli, W. W. Schultz, and B. S. Sack. Ultrasound contrast stability for urinary bladder pressure measurement. *Ultrasound Med. Biol.*, 49(1):136–151, 2023.

[9] T. Yamaguchi. Basic concept and clinical applications of quantitative ultrasound (qus) technologies. *J. Med. Ultrason.*, 48(4):391–402, 2021.

[10] N. Renaudin, C. Demené, A. Dizeux, N. Ialy-Radio, S. Pezet, and M. Tanter. Functional ultrasound localization microscopy reveals brain-wide neurovascular activity on a microscopic scale. *Nat. Methods*, 19(8):1004–1012, 2022.

[11] Y. Meng, K. Hynynen, and N. Lipsman. Applications of focused ultrasound in the brain: From thermoablation to drug delivery. *Nat. Rev. Neurol.*, 17(1):7–22, 2021.

[12] S. Liang, B. E. Treeby, and E. Martin. Review of the low-temperature acoustic properties of water, aqueous solutions, lipids, and soft biological tissues. *IEEE Trans. Ultrason. Ferroelectr. Freq. Control*, 2024.

[13] B. M. Howe, J. Miksis-Olds, E. Rehm, H. Sagen, P. F. Worcester, and G. Haralabus. Observing the oceans acoustically. *Front. Mar. Sci.*, 6:426, 2019.

[14] S. Giwa, J. K. Lewis, L. Alvarez, R. Langer, A. E. Roth, G. M. Church, J. F. Markmann, D. H. Sachs, A. Chandraker, J. A. Wertheim, et al. The promise of organ and tissue preservation to transform medicine. *Nat. Biotechnol.*, 35(6):530–542, 2017.

[15] L. Qiu, M. Zhang, B. Chitrakar, and B. Bhandari. Application of power ultrasound in freezing and thawing processes: Effect on process efficiency and product quality. *Ultrason. Sonochem.*, 68:105230, 2020.

[16] N. Bhargava, R. S. Mor, K. Kumar, and V. S. Sharanagat. Advances in application of ultrasound in food processing: A review. *Ultrason. Sonochem.*, 70:105293, 2021.

[17] C. Cadot, J.-F. Saillant, and B. Dulmet. Method for acoustic characterization of materials in temperature. In *Proc. 19th World Conf. Non-Destruct. Test.*, 2016.

[18] S. Pal, F.-S. Lin, C.-C. Hsieh, M.-C. Huang, C.-Y. Lee, Y.-H. Liu, C.-Y. Lu, S.-W. Du, and C.-H. Huang. Acoustic speed measurement platform for monitoring highly concentrated gas temperature distribution. *IEEE Sens. Lett.*, 6(3):1–4, 2022.

[19] B. Zeqiri, W. Scholl, and S. P. Robinson. Measurement and testing of the acoustic properties of materials: A review. *Metrologia*, 47(2):S156, 2010.

[20] G. R. Harris, S. M. Howard, A. M. Hurrell, P. A. Lewin, M. E. Schafer, K. A. Wear, V. Wilkens, and B. Zeqiri. Hydrophone measurements for biomedical ultrasound applications: A review. *IEEE Trans. Ultrason. Ferroelectr. Freq. Control*, 70(2):85–100, 2022.

[21] S. Rajagopal, N. Sadhoo, and B. Zeqiri. Reference characterisation of sound speed and attenuation of the iec agar-based tissue-mimicking material up to a frequency of 60 mhz. *Ultrasound Med. Biol.*, 41(1):317–333, 2015.

[22] S. Hoche, M. A. Hussein, and T. Becker. Ultrasound-based density determination via buffer rod techniques: A review. *J. Sens. Sens. Syst.*, 2(2):103–125, 2013.

[23] E. Bjorndal and K.-E. Froysa. Acoustic methods for obtaining the pressure reflection coefficient from a buffer rod based measurement cell. *IEEE Trans. Ultrason. Ferroelectr. Freq. Control*, 55(8):1781–1793, 2008.

[24] T. Ihara, N. Tsuzuki, and H. Kikura. Development of the ultrasonic buffer rod for the molten glass measurement. *Prog. Nucl. Energy*, 82:176–183, 2015.

[25] Y. Liu, L. J. Bond, and H. Hu. Ultrasonic-attenuation-based technique for ice characterization pertinent to aircraft icing phenomena. *AIAA J.*, 55(5):1602–1609, 2017.

[26] J. L. Jordan, R. L. Rowland, J. Greenhall, E. K. Moss, R. C. Huber, E. C. Willis, R. Hrubiak, C. Kenney-Benson, B. Bartram, and B. T. Sturtevant. Elastic properties of polyethylene from high pressure sound speed measurements. *Polymer*, 212:123164, 2021.

[27] E. P. Papadakis, K. A. Fowler, and L. C. Lynnworth. Ultrasonic attenuation by spectrum analysis of pulses in buffer rods: Method and diffraction corrections. *J. Acoust. Soc. Am.*, 53(5):1336–1343, 1973.

[28] N. Hoppe, A. Puttmer, and P. Hauptmann. Optimization of buffer rod geometry for ultrasonic sensors with reference path. *IEEE Trans. Ultrason. Ferroelectr. Freq. Control*, 50(2):170–178, 2003.

[29] J. García-Álvarez, M. J. García-Hernández, D. F. Novoa-Díaz, A. Turó Peroy, J. A. Chávez Domínguez, and J. Salazar Soler. Resizing buffer rods for ultrasound testing of food products with acoustic noise considerations. *Ultrasonics*, 53(1):294–301, 2013.

[30] E. Bjorndal, K.-E. Froysa, and S.-A. Engeseth. A novel approach to acoustic liquid density measurements using a buffer rod based measuring cell. *IEEE Trans. Ultrason. Ferroelectr. Freq. Control*, 55(8):1794–1808, 2008.

[31] V. A. Del Grosso. Systematic errors in ultrasonic propagation parameter measurements. part 2. effects of guided cylindrical modes. Technical report, Naval Research Lab, Sound Division, Propagation Branch, Washington, 1965.

[32] E. R. Generazio. The role of the reflection coefficient in precision measurement of ultrasonic attenuation. Technical report, National Aeronautics and Space Administration, Lewis Research Center, 1984.

[33] R. Xu, B. E. Treeby, and E. Martin. Experiments and simulations demonstrating the rapid ultrasonic rewarming of frozen tissue cryovials. *J. Acoust. Soc. Am.*, 153(1):517–528, 2023.

[34] E. Alcalá, L. Encabo, F. Barroso, A. Puentes, I. Risco, and R. Risco. Sound waves for solving the problem of recrystallization in cryopreservation. *Sci. Rep.*, 13(1):7603, 2023.

[35] M. Bakaric, P. Miloro, A. Javaherian, B. T. Cox, B. E. Treeby, and M. D. Brown. Measurement of the ultrasound attenuation and dispersion in 3d-printed photopolymer materials from 1 to 3.5 mhz. *J. Acoust. Soc. Am.*, 150(4):2798–2805, 2021.

[36] L. E. Kinsler, A. R. Frey, A. B. Coppens, and J. V. Sanders. *Fundamentals of acoustics*. John Wiley & Sons, 2000.

[37] R. T. Higuti and J. C. Adamowski. Ultrasonic densitometer using a multiple reflection technique. *IEEE Trans. Ultrason. Ferroelectr. Freq. Control*, 49(9):1260–1268, 2002.

[38] R. F. O'Doherty and N. A. Anstey. Reflections on amplitudes. *Geophys. Prospect.*, 19(3):430–458, 1971.

[39] Onda Corporation. Information on the acoustic properties of plastics. `https://www.ondacorp.com/wp-content/uploads/2020/09/Plastics.pdf`, 2022. Last viewed January 24, 2025.

[40] D. Marioli, C. Narduzzi, C. Offelli, D. Petri, E. Sardini, and A. Taroni. Digital time-of-flight measurement for ultrasonic sensors. *IEEE Trans. Instrum. Meas.*, 41(1):93–97, 1992.

[41] K. W. Nowak and M. Markowski. A comparison of methods for the determination of sound velocity in biological materials: A case study. *Ultrasonics*, 53(5):923–927, 2013.

[42] J. M. M. Pinkerton. The absorption of ultrasonic waves in liquids and its relation to molecular constitution. *Proc. Phys. Soc. B*, 62(2):129, 1949.

[43] B. E. Treeby and B. T. Cox. k-wave: Matlab toolbox for the simulation and reconstruction of photoacoustic wave fields. *J. Biomed. Opt.*, 15(2):021314–021314, 2010.

[44] B. E. Treeby, B. T. Cox, E. Z. Zhang, S. K. Patch, and P. C. Beard. Measurement of broadband temperature-dependent ultrasonic attenuation and dispersion using photoacoustics. *IEEE Trans. Ultrason. Ferroelectr. Freq. Control*, 56(8):1666–1676, 2009.

[45] W. Marczak. Water as a standard in the measurements of speed of sound in liquids. *J. Acoust. Soc. Am.*, 102(5):2776–2779, 1997.

[46] ISO-25178-700. Geometrical product specifications (GPS)—Surface texture: Areal—Part 700: Calibration, adjustment and verification of areal topography measuring instruments. Standard, International Organization for Standardization, dec 2022.

[47] Les Kirkup and Robert B Frenkel. *An introduction to uncertainty in measurement: using the GUM (guide to the expression of uncertainty in measurement)*. Cambridge University Press, 2006.

[48] Sławomir Suchoń, Michał Burkacki, Miłosz Chrzan, and Mateusz Winder. What ranges of probe pressure are applied during ultrasound examinations? a systematic review. *Sensors*, 25(11):3415, 2025.

[49] J. Salvi, S. Fernandez, T. Pribanic, and X. Llado. A state of the art in structured light patterns for surface profilometry. *Pattern Recognit.*, 43(8):2666–2680, 2010.

[50] Q. Zhou, K. H. Lam, H. Zheng, W. Qiu, and K. K. Shung. Piezoelectric single crystal ultrasonic transducers for biomedical applications. *Prog. Mater. Sci.*, 66:87–111, 2014.

[51] M. Ragozzino. Analysis of the error in measurement of ultrasound speed in tissue due to waveform deformation by frequency-dependent attenuation. *Ultrasonics*, 19(3):135–138, 1981.

[52] K. Ono. A comprehensive report on ultrasonic attenuation of engineering materials, including metals, ceramics, polymers, fiber-reinforced composites, wood, and rocks. *Appl. Sci.*, 10(7):2230, 2020.

[53] Julian L Davis. *Wave propagation in solids and fluids*. Springer Science & Business Media, 2012.

[54] Josef Krautkrämer and Herbert Krautkrämer. Plane sound waves at boundaries. In *Ultrasonic Testing of Materials*, pages 15–45. Springer, 1990.

[55] Hongchen Miao and Faxin Li. Shear horizontal wave transducers for structural health monitoring and nondestructive testing: A review. *Ultrasonics*, 114:106355, 2021.

[56] HR López-Cabrera, U Figueroa-López, and A Guevara-Morales. Determining polyamide dynamic fracture resistance under plane strain conditions by high-speed double torsion tests. *SPE Polymers*, 6(2):e70006, 2025.

[57] Kanji Ono. Dynamic viscosity and transverse ultrasonic attenuation of engineering materials. *Applied Sciences*, 10(15):5265, 2020.